LETTER

Experimental Discovery of a Fast and Stable Lithium Thioborate Solid Electrolyte, $Li_{6+2x}[B_{10}S_{18}]S_x$ ($x \approx 1$)

Yinxing Ma,[†] Jiayu Wan,[†] Xin Xu,[†] Austin D. Sendek, Sarah E. Holmes, Brandi Ransom, Zhelong Jiang, Pu Zhang, Xin Xiao, Wenbo Zhang, Rong Xu, Fang Liu, Yusheng Ye, Emma Kaeli, Evan J. Reed,* William C. Chueh,* and Yi Cui*

Read Online

ACCESS | Metrics & More | Article Recommendations | SI Supporting Information

ABSTRACT: High-performance, practical all-solid-state batteries (ASSBs) require solid-state electrolytes (SSEs) with fast Li-ion conduction, wide electrochemical stability window, low cost, and low mass density. Recent density functional theory (DFT) simulations have suggested that lithium thioborates are a particularly promising class of materials for high-performance SSEs in Li batteries, but these materials have not been studied extensively experimentally due to synthesis difficulty. Particularly, their electrochemical properties remain largely underexplored, limiting their further development and application as SSEs. In this work, we report the successful synthesis and a comprehensive electrochemical performance study of single-phase, crystalline $Li_{6+2x}[B_{10}S_{18}]S_x$ ($x \approx 1$). We find cold-pressed samples of $Li_{6+2x}[B_{10}S_{18}]S_x$ ($x \approx 1$) to exhibit a high ionic conductivity of 1.3×10^{-4} S cm^{-1} at room temperature. Furthermore, $Li_{6+2x}[B_{10}S_{18}]S_x$ ($x \approx 1$) shows an electrochemical stability window of 1.3−2.5 V, much wider than most sulfide SSEs. Symmetrical Li−Li cells fabricated with a $Li_{6+2x}[B_{10}S_{18}]S_x$ ($x \approx 1$) pellet were cycled up to a current density of 1 mA cm^{-2} and exhibited good long-term cycling stability for more than 140 h at 0.3 mA cm^{-2}. These results suggest $Li_{6+2x}[B_{10}S_{18}]S_x$ ($x \approx 1$) as a promising choice of SSE for high-performance ASSBs for energy storage.
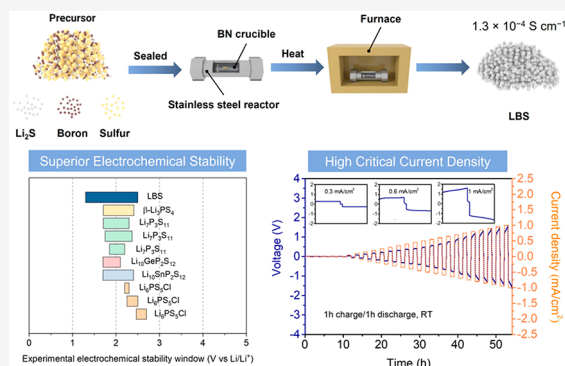
Li metal batteries (LMBs) represent one of today's most extensively studied electrochemical energy storage technologies due to the high specific capacity of Li metal anodes (~3860 mAh/g),[1,2] which could enable significantly higher energy density. Compared with traditional liquid electrolytes-based LMBs with safety risks due to the volatility and flammability of the organic solvents, all-solid-state batteries (ASSBs) have attracted tremendous attention in both academia and industry due to potential improvements in safety as well as higher energy density and wider operating temperature range.[3−8] Solid-state electrolytes (SSEs) are essential components in ASSBs,[4,9] but the rational design of new electrolytes represents a significant scientific challenge. A high-performance solid electrolyte must simultaneously exhibit fast Li-ion conduction, a wide electrochemical stability window, and mechanical resistance against lithium penetration.[4,10−12] Decreasing the cost and weight will also ensure economic competitiveness and high energy density.[13,14]

Among various SSEs, sulfide solid electrolytes[15−19] (e.g., lithium thiophosphates (LPS)) are promising candidates to

satisfy the combination of these properties due to their high ionic conductivity, some ductility, and low mass density.[15,18,20,21] However, traditional sulfide SSEs tend to have a narrow electrochemical stability window,[22,23] limiting the operation voltages of full cells. Recently, four lithium thioborate phases were predicted through density functional theory (DFT) computation and grand potential phase analysis to exhibit ultrahigh single-crystal ionic conductivities, wide electrochemical stability windows, low cost, and low mass density simultaneously, comparable to or exceeding those of the best-known oxide ceramic electrolyte materials.[24] However,
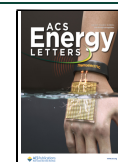
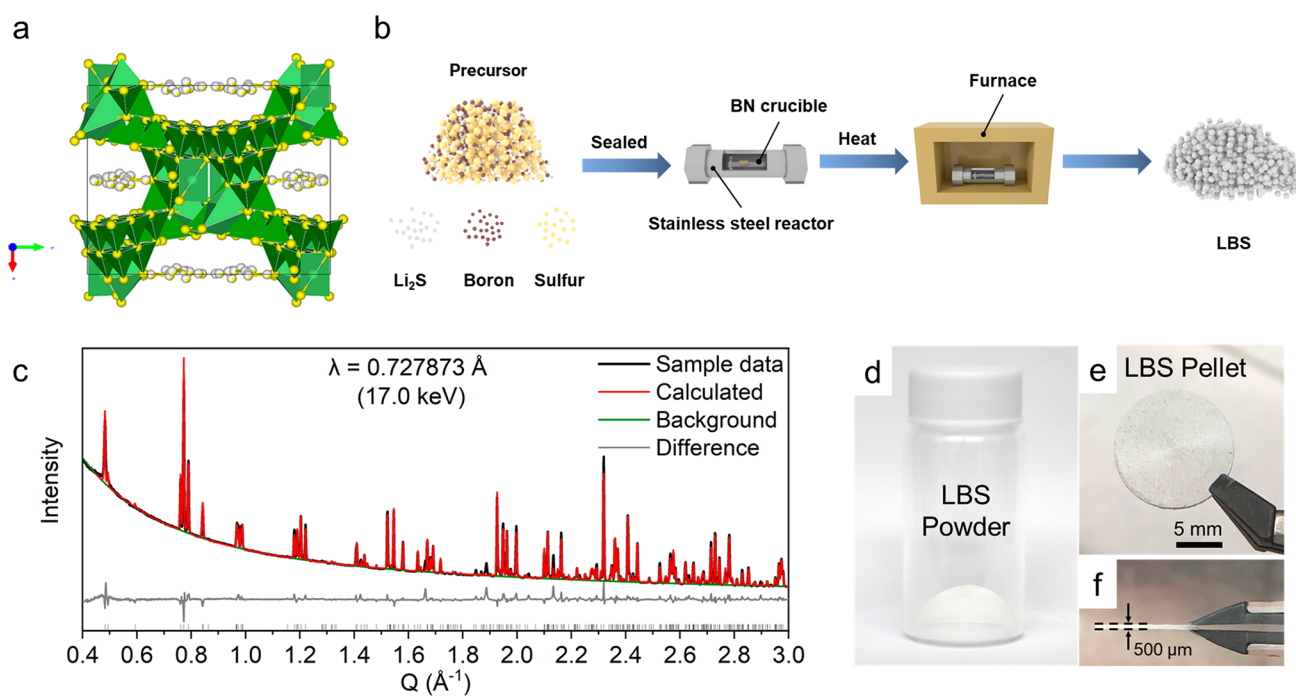**Figure 1.** (a) Crystal structure of $Li_{6+2x}[B_{10}S_{18}]S_x$ ($x \approx 1$ or 2) (BS_4: green tetrahedra, S: yellow spheres, Li: omitted). (b) Schematic illustration of the synthesis of the LBS powder. (c) Synchrotron XRD pattern of the material with its Rietveld refinement result. Experimental data is shown in the black line; the calculated pattern is shown in red with the background as green; the difference between data and calculation is displayed in gray. The tick marks at the bottom indicate calculated Bragg peak positions. (d) Photo image of LBS powder. (e, f) Photo image of the LBS pellet from (e) top view and (f) side view. The LBS pellet was prepared by pressing LBS powder under 360 MPa for 2 min. The pellet exhibits a large diameter of 13 mm and a thin thickness of ~500 μm.

to date, these materials have been rarely studied experimentally due to the difficulty in the synthesis of pure materials.

The known lithium thioborate (Li-B-S) materials include $Li_5B_7S_{13}$,[25,26] Li_3BS_3,[27,28] $Li_9B_{19}S_{33}$,[26] $Li_2B_2S_5$,[29] and $Li_{10}B_{10}S_{20}$.[30] The $Li_{10}B_{10}S_{20}$ phase was first synthesized and reported as $Li_{6+2x}[B_{10}S_{18}]S_x$ ($x \approx 2$) in 1990.[30] Briefly, $Li_{6+2x}[B_{10}S_{18}]S_x$ ($x \approx 1$ or 2) constitutes a ternary chalcogenide structure composed of a well-defined rigid polymeric thioborate framework of composition $[B_{10}S_{18}^{6-}]_n$ and a highly disordered system composed of around $(6 + 2x)$ Li^+ and x S^{2-} ions per formula unit (Figure 1 a). Ten parallel BS_4 tetrahedra are connected by their corner S atoms to form a 3D macro-tetrahedral/super-adamantanoid $B_{10}S_{20}$ cluster. Each $B_{10}S_{20}$ macro-tetrahedron is further connected by all four of its corner S atoms to adjacent macro-tetradedra, forming two interpenetrating but nonbonding networks with composition of $[B_{10}S_{18}^{6-}]_n$. As evident in Figure 1a, large voids exist within this $[B_{10}S_{18}^{6-}]_n$ framework, creating channels that host highly disordered sites for the nonframework S ions and the majority of the Li ions.

In the original work by Hebel and Krebs, the product synthesized may have contained a significant fraction of $Li_5B_7S_{13}$ and Li_3BS_3 impurities. ^{7}Li NMR studies of the lithium dynamics revealed a low activation energy of 12 kJ/mol (equivalent to 0.12 eV),[30] implying that this thioborate phase is a superionic conductor. Nevertheless, such a high ionic conductivity was not experimentally verified via transport measurements. Additionally, the electrochemical properties of this phase—or any of the Li-B-S phases, for that matter—were rarely studied for solid electrolytes or batteries. Recently, Nazar and colleagues synthesized and characterized the ionic conductivity of three lithium-ion conducting materials

prepared by full substitution of S^{2-} with monovalent X^- (Cl^-, Br^-, and I^-) to form lithium thioborate halides.[20] While these compounds exhibit attractive ionic conductivity, other electrochemical properties such as stability were not determined.

In this work, we used a solid-state reaction to synthesize single-phase crystalline $Li_{6+2x}[B_{10}S_{18}]S_x$ ($x \approx 1$). Hereinafter, we refer to $Li_{6+2x}[B_{10}S_{18}]S_x$ ($x \approx 1$) as LBS. Our approach diverges from the original method reported by Hebel and Krebs.[30] After carefully optimizing synthesis parameters including the ratio of raw materials, synthesis atmosphere, temperature, and duration, we successfully achieved single-phase crystalline LBS without any other Li-B-S phase impurities. We then comprehensively studied the electrochemical performance of LBS. Specifically, LBS shows an ionic conductivity of 1.3×10^{-4} S cm^{-1} at room temperature (RT). Excitingly, LBS has an electrochemical stability window of 1.3−2.5 V against metallic Li, which is substantially wider than those of most sulfide system electrolytes.[22,31] Symmetrical Li−Li cells with LBS SSE did not short circuit even when the current density reached 1 mA cm^{-2} with a cycling capacity of 1 mAh cm^{-2} at RT. At a current density of 0.3 mA cm^{-2} and a cycling capacity of 0.3 mAh cm^{-2}, the cells cycled for more than 140 h. The improved critical current density and cycling stability indicate that LBS exhibits notable Li dendrite suppression, which may enable ASSBs with increased power density.[32] Furthermore, the ionic conductivity of LBS appears to be stable. Our work provides a comprehensive analysis on the electrochemical performance and battery performance of lithium thioborates. It provides a new type of sulfide solid electrolyte for inorganic solid electrolytes, opening the door to the study of a new class of lithium thioborates SSE.
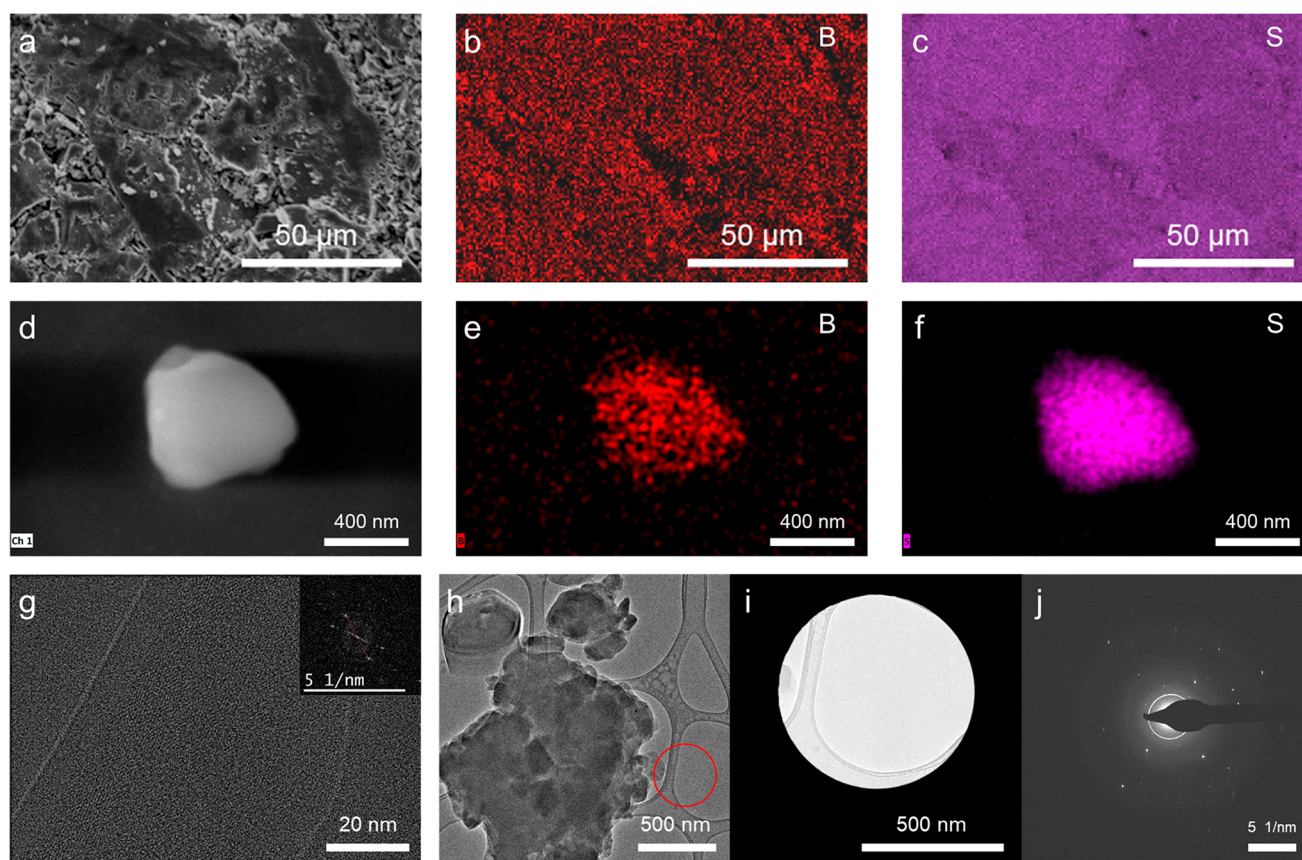
Figure 2. (a) SEM image of the LBS pellet surface. (b, c) Corresponding EDX images of the LBS pellet surface: (b) distribution of B and (c) distribution of S. (d) SEM image of the LBS particle. (e, f) Corresponding EDX images of the LBS particle: (e) distribution of B and (f) distribution of S. (g) High-resolution cryo-TEM image of a LBS particle (inset shows FFT). (h–j) SADP images of the LBS particle.

The solid-state reaction is illustrated in Figure 1b. First, Li_2S, boron powder, and sulfur powder with an appropriate ratio are mixed in an Ar-filled glovebox to obtain a uniform precursor mixture. Next, the precursor mixture is loaded into a boron nitride (BN) crucible, which is sealed in a stainless-steel reactor. The reactor is then taken out of the glovebox for heating. Finally, the reactor is opened in the glovebox to collect the LBS powder. In contrast to the previously reported LBS synthesis which took several days, our whole procedure, including cooling, took 32 h, ensuring high synthesis efficiency. The Li/B ratio was determined by inductively coupled plasma mass spectrometry (ICP-MS) spectroscopy to be 0.80 ± 0.01:1.

The X-ray diffraction (XRD) pattern of the synthesized sample is shown in Figure 1c (black line). The diffraction pattern can be well indexed to a monoclinic unit cell with a = 21.05291(16) Å, b = 21.16732(16) Å, c = 16.18522(11) Å, and β = 128.3917(4)°. There are no unaccountable peaks, and the lattice parameters are very close to those of the initial single-crystal solution of $Li_{6+2x}[B_{10}S_{18}]S_x$ ($x \approx 2$) from Hebel and Krebs,[30] indicating a single-phase crystalline product with the same $[B_{10}S_{18}^{6-}]_n$ framework was obtained. Rietveld refinement of the data was performed with a crystal structure model derived from the original solution from Hebel and Krebs,[30] and the result is shown in Figure 1c (details about refinement and structure are discussed in the Supporting Information, Figure S1 and Table S1). Reasonable agreement between the experimental and calculated patterns is achieved. The minor misfit intensities cannot be explained by any known Li-B-S

phases and are attributed to the intrinsic nature of this material. It has highly disordered nonframework S and Li atoms, whose coordinates and occupancy are unconstrained and challenging to refine even from single-crystal diffractions.[20,30] Such highly dispersive nonframework atomic sites contribute to the high Li mobility within the material, which we discuss later.

The synthesis atmosphere, ratio of raw materials, heating temperatures, and duration all affect the product phases (Table S2 in the Supporting Information). To obtain single-phase crystalline LBS, the following conditions need to be satisfied: Ar atmosphere instead of vacuum, excess boron and sulfur with an appropriate ratio, heating profile of 750 °C for 2 h and 550 °C for 12 h. As shown in Figure 1d, LBS shows white color. The powder can be easily pressed into a large, thin pellet with a diameter of 13 mm (Figure 1e) and a thickness of ∼500 μm (Figure 1f), which ensures good processability and high energy density in ASSBs.

The scanning electron microscopy (SEM) image of the LBS pellet surface is shown in Figure 2a. The corresponding energy-dispersive X-ray spectroscopy (EDX) images (Figure 2b,c) show the even distribution of boron and sulfur, indicating the good uniformity of LBS. The SEM image and EDX images of a single particle also exhibit uniform distribution of boron and sulfur (Figure 2d–f). We note that LBS is sensitive to the electron. As shown in Figure S2, obvious beam damage could be observed on the same particle after focusing for 1 and 2 min. Therefore, to avoid this issue, we carried out transmission electron microscopy (TEM) at cryogenic conditions. The low-
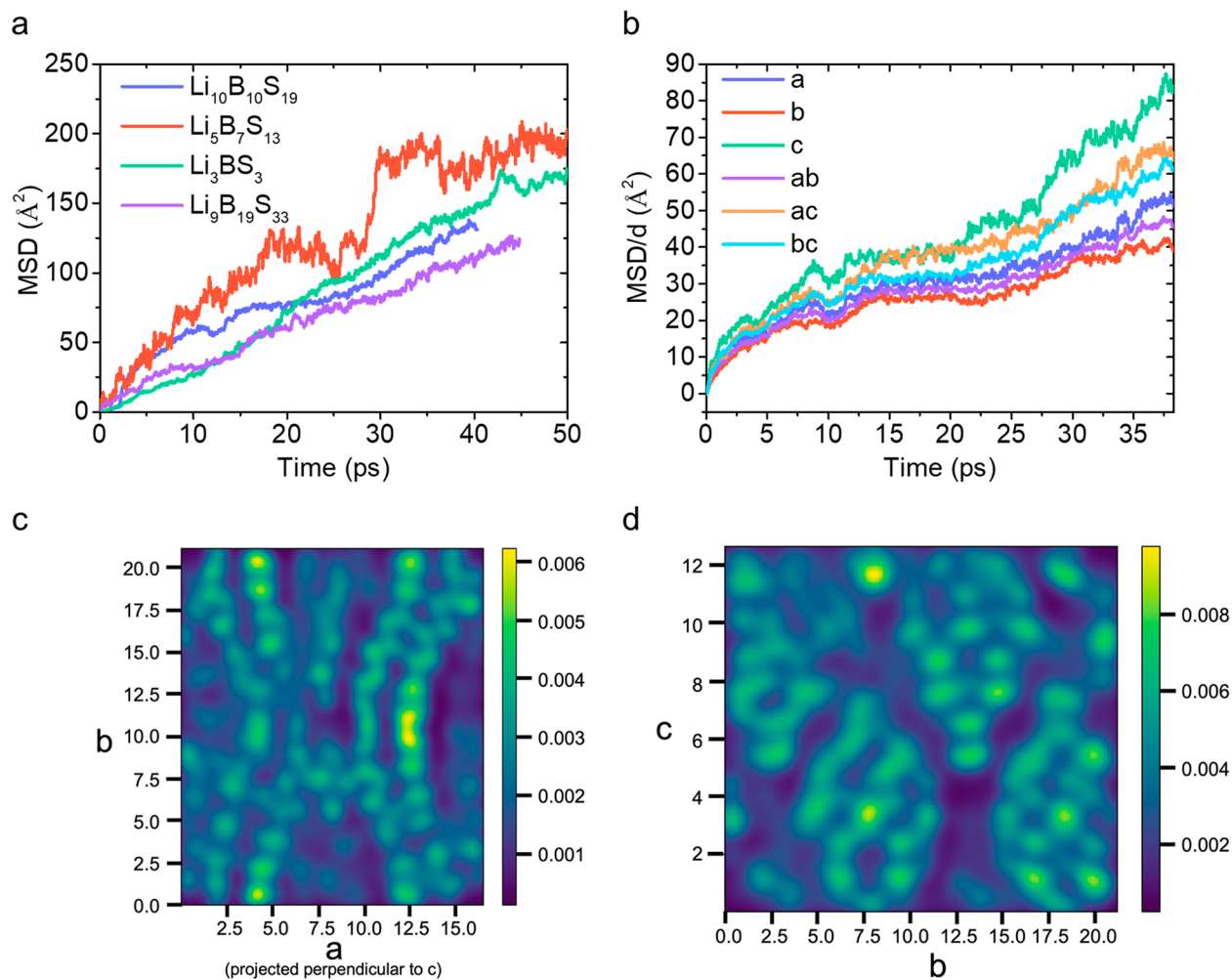
Figure 3. (a) Comparing the mean-squared displacement (MSD) of Li over 40−50 ps of DFT-MD simulation in $Li_{10}B_{10}S_{19}$ and other Li-B-S phases suggests this phase will exhibit fast ionic conductivity like the others. (b) Li MSD along the directions (*a*, *b*, *c*) and planes (*ab*, *bc*, *ac*) defined by the lattice vectors suggests Li diffusion is favored in the *c* direction and associated places (*ac*, *bc*). Note the *y* axis shows the MSD normalized by the dimensionality *d* to facilitate direct comparisons of the diffusivities; *d* = 1 for the *a*, *b*, and *c* MSDs and *d* = 2 for the *ab*, *bc*, and *ac* MSDs. (c) Heatmaps of the Li probability density looking along the *c* direction. (d) Li probability density onto the *bc* plane. These heatmaps suggest Li diffusion occurs along the exteriors of the polymeric $[B_{10}S_{18}{}^{6-}]$ structures and not through the open channels.

dose, high-resolution cryo-TEM image of a LBS particle is shown in Figure S3, where the phase contrast of the atomic lattice shows high crystallinity in the high-magnification image (Figure 2g). The inset fast Fourier transform (FFT) shows the atomic lattice has a *d*-spacing of 8.13 Å, corresponding to the (0 2 1) atomic plane of LBS. Selected area diffraction pattern (SADP) images were obtained from the area selected in Figure 2h,i. The spots correspond to *d*-spacings of 3.17 Å, 2.31 Å, and 3.68 Å (Figure 2j; more details are shown in Figure S4) and to different atomic planes of (2 4 2), (1 7 3), and (−5 1 4), respectively, consistent with XRD data. Furthermore, the electron energy loss spectroscopy (EELS) data also confirms the uniform distribution of lithium, boron, and sulfur (Figure S5).

We perform density functional theory molecular dynamics (DFT-MD) simulations of Li ion diffusion to identify the primary conduction pathways. Because nonstoichiometric compositions tend to exhibit higher ionic conductivities than stoichiometric compositions, we simulate Li ion diffusion in $Li_{10}B_{10}S_{19}$, a Li-rich variant of the $Li_8B_{10}S_{19}$ structure. This is done to facilitate diffusion so that conduction pathways may be observed on computationally tractable time scales; we do not

seek to compute an exact ionic conductivity value. We run DFT-MD at 900 K for approximately 40 ps using the NVT canonical ensemble. Due to the very large 312-atom primitive cell, it is intractable to generate hundreds of picoseconds or more of MD data as is commonly done to compute the ionic conductivities of crystalline materials.[24,33] We observe a Li mean-squared displacement (MSD) of more than 100 Å² over the 40 ps simulation, on par with previously reported computational results for other Li-B-S phases over a comparable amount of simulation time: $Li_9B_{19}S_{33}$, $Li_5B_7S_{13}$, and Li_3BS_3 (Figure 3a).[24]

$Li_8B_{10}S_{19}$ has a complex structure with a large primitive cell that likely supports many diffusion mechanisms. To probe where Li conducts most rapidly, we construct heatmaps showing the trajectories most commonly occupied by Li (Figure 3c,d). These heatmaps suggest Li tends to conduct along the outside of the polymeric $[B_{10}S_{18}{}^{6-}]$ structures and does not traverse the open channels between these structures. Computing the Li MSD along the directions of the *a*, *b*, and *c* lattice vectors, and the *ab*, *bc*, and *ac* planes, suggests Li diffuses in all directions but is not entirely isotropic; diffusion along the *c* direction and in the *bc* and *ac* planes is favored, while the
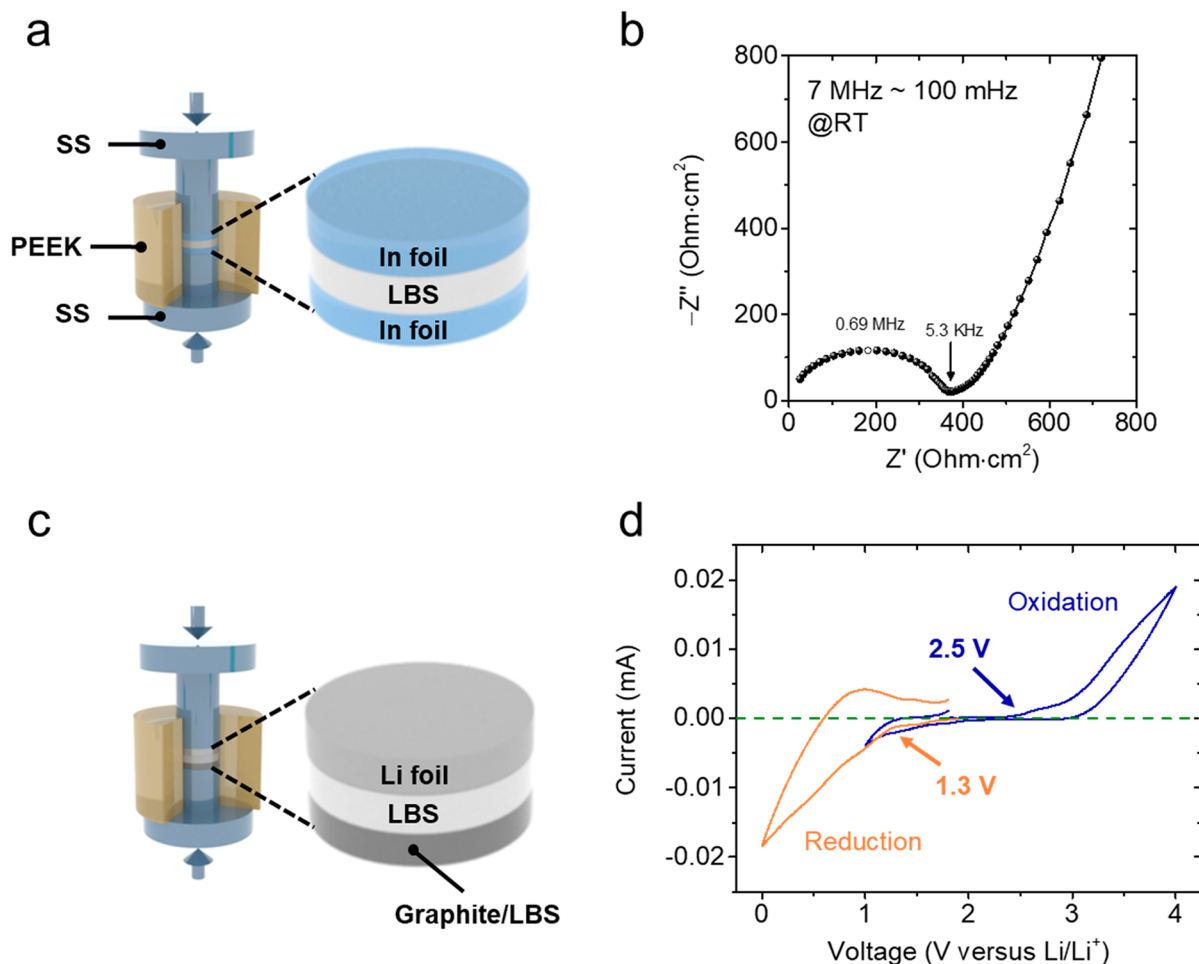
Figure 4. (a) Schematic illustration of In/LBS/In cell configuration for ionic conductivity measurement. (b) Impedance spectra of LBS pellet. (c) Schematic illustration of Li/LBS/LBS-graphite cell configuration for cyclic voltammetry measurement. (d) Cyclic voltammetry curves of Li/LBS/LBS-graphite cell within the voltage ranges of 1−4 V and 0−1.8 V at a scan rate of 0.1 mV/s at RT.

magnitude of the diffusion along the *a* and *b* directions is lower by about one-third to one-half (Figure 3b). To directly compare the one- and two-dimensional MSDs, we normalize the MSD values in Figure 3b by the dimensionality *d*, where *d* = 1 for the *a*, *b*, and *c* MSDs and *d* = 2 for the *ab*, *bc*, and *ac* MSDs. To visualize the conduction pathways, we visualize heatmaps collapsing the three-dimensional Li probability density down onto two planes: one perpendicular to the *c* lattice vector (Figure 3c) and the *bc* plane (Figure 3d). These heatmaps show a conspicuous absence of Li intensity in the gaps between the polymeric $[B_{10}S_{18}{}^{6-}]$ structures, suggesting Li diffuses along the outside of the structures but does not cross the gaps between neighboring structures.

The electrochemical properties of LBS were characterized in customized pressure-controlled cells. For ionic conductivity measurement, two indium (In) foils were placed on each side of a LBS pellet in an In/LBS/In cell (Figure 4a). The impedance spectra are typical of an ionic conductor (Figure 4b),[32] indicating an ionic conductivity of 1.3×10^{-4} S cm^{-1}.

A wide electrochemical stability window is desired to enable the highest voltage output of the solid-state battery by coupling a lithium metal anode with a high-voltage cathode material.[34,35] We note that many works have employed Li/SSE/platinum cells to characterize the electrochemical stability window, claiming a wide window of 0−5 V[17,34,36] and even a higher voltage upper limit of 10 V.[37,38] However, the above-

mentioned method is not accurate because the decomposition current is overshadowed by the huge Li deposition/dissolution peaks[34,35] and the electrolyte/electrode contact area is small. To avoid the huge Li deposition/dissolution peaks, the cyclic voltammetry (CV) needs to be scanned within restricted voltage windows.[22,35] As a result, to characterize the electrochemical stability of LBS, we carried out CV tests on Li/LBS/LBS-graphite cells (Figure 4c). Graphite was mixed into LBS to form a composite electrode. The increased contact between SSE and graphite improves the kinetics of the decomposition reaction due to the facile electron transport as well as significantly increased active area for the charge-transfer reaction.[22,34,35] CV was scanned between 1 and 4 V to test the oxidation of LBS. We observed oxidation starting at 2.5 V (Figure 4d). For LBS reduction, we scanned between 0 and 1.8 V. There, the reduction starts at 1.3 V (Figure 4d). Therefore, the electrochemical stability window of LBS is 1.3−2.5 V. This window is considerably wider than those of the majority of sulfide solid electrolytes (Figure S6)[35,39−46] such as β-Li$_3$PS$_4$, Li$_7$P$_3$S$_{11}$, Li$_{10}$GeP$_2$S$_{12}$, Li$_{10}$SnP$_2$S$_{12}$, and Li$_6$PS$_5$Cl within the Li|SSE|SSE+C test cell configuration. To ensure a fair comparison, we specifically chose pristine sulfide electrolytes (without any dopants or coatings) and determined the range of the electrochemical stability window based on the onset voltage.
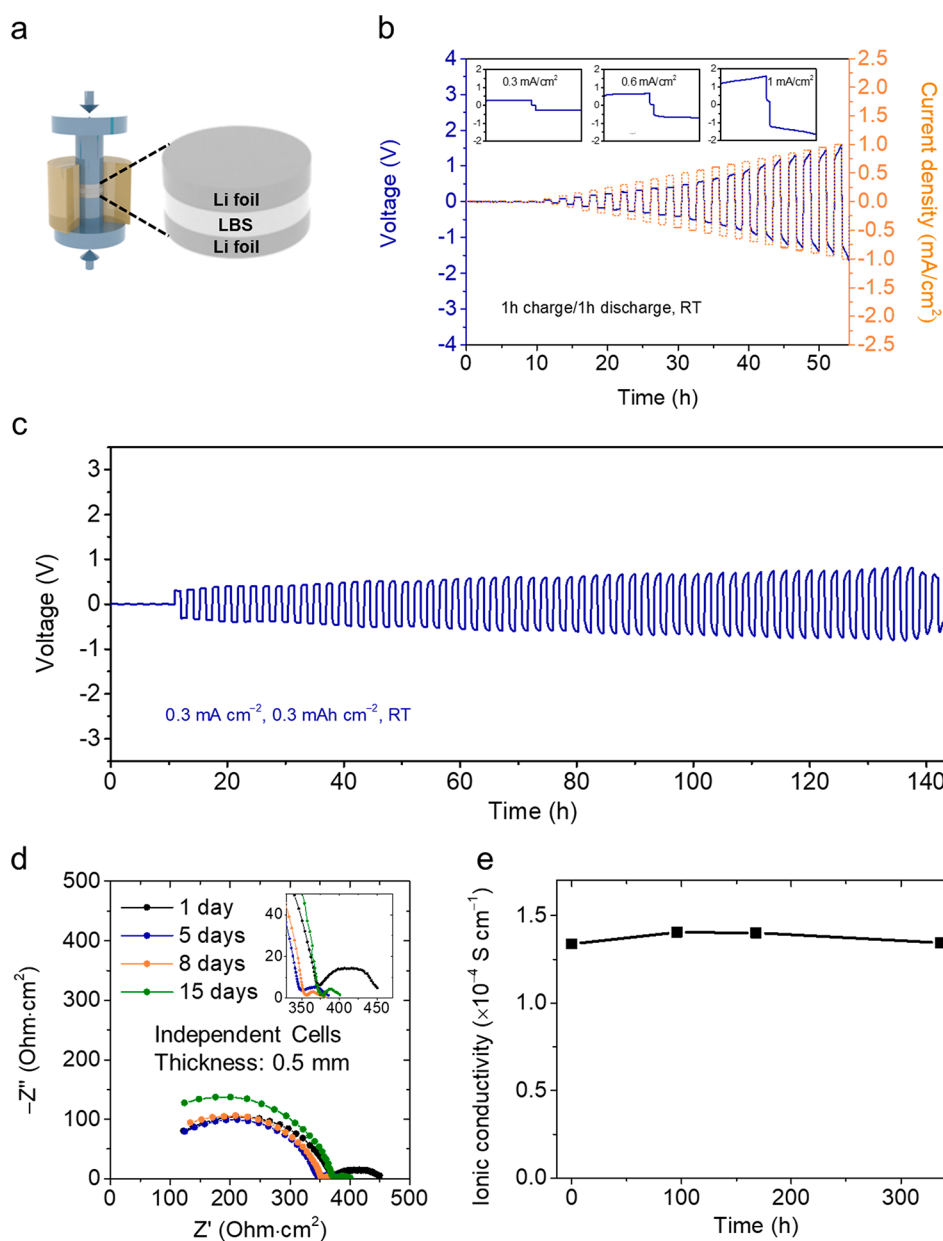
Figure 5. (a) Schematic illustration of a symmetrical Li/LBS/Li cell. (b) Galvanostatic cycling of the Li/LBS/Li cell at step-increased current densities at RT under a cycling pressure of 35 MPa. The time for each charge and discharge is 1 h. The step size for the current increase is 0.05 mA cm^{-2}. Insets: voltage profile of Li/LBS/Li at 0.3, 0.6, and 1.0 mA cm^{-2}, respectively. (c) Galvanostatic cycling at 0.3 mA cm^{-2} of the Li/LBS/Li cell at RT under a cycling pressure of 35 MPa. The time for each charge and discharge is 1 h. (d) Impedance spectra of the LBS pellet after storage for different numbers of days, measured in symmetrical Li/LBS/Li cells. Inset shows the interfacial resistance. (e) Ionic conductivity of the LBS pellet after storage for different times.

To demonstrate the LBS's performance in a symmetrical cell configuration at RT, we fabricated Li/LBS/Li cells (Figure 5a). The critical current density is an important factor for Li−Li cells and is defined as the highest current density symmetrical Li−Li cells can withstand before failure (short circuiting or drastic overpotential increase).[47] As shown in Figure 5b, the critical current density of LBS reached 1 mA cm^{-2} with a charge/discharge capacity of 1 mAh cm^{-2}. Another symmetrical Li−Li cell was run at 0.3 mA cm^{-2} with a charge/discharge capacity of 0.3 mAh cm^{-2} for long-term cycling at RT (Figure 5c). The cell operates for more than 140 h, showing good cycling performance. The high critical current density and good long-term cycling stability indicate that LBS

exhibits good Li dendrite suppression capability and may be useful in high-power Li metal batteries.

Finally, the LBS solid-state electrolyte showed good stability in ionic conductivity. The ionic conductivity of LBS was measured in symmetrical Li−Li cells after storage in a glovebox between 1 and 15 days at RT. The impedance spectra overlap with one another (Figure 5d). The ionic conductivity at different times was calculated (Figure 5e), showing good stability with time. No decrease in ionic conductivity was observed after more than 2 weeks. Besides, the interfacial resistance shown in the impedance spectra decreased after the first measurement and remained unchanged over time, which indicates a stable solid−electrolyte interface is likely formed (Figure 5d, inset). This indicates that the LBS SSE has good

stability and limited reduction against Li/Li$^+$ over time, ensuring suitability for long-term storage and use.

In summary, we successfully synthesized a new lithium thioborate SSE, Li$_{6+2x}$[B$_{10}$S$_{18}$]S$_x$ ($x \approx 1$) (LBS), through a solid-state reaction and studied its electrochemical properties through a combination of experimentation and simulation. LBS offers a crystalline single phase, high purity, good uniformity, low density, good processability, and high synthesis efficiency. LBS exhibits high ionic conductivity and a wide electrochemical stability window of 1.3−2.5 V. Furthermore, cycling in symmetrical Li/LBS/Li cells demonstrates a high critical current density of 1 mA cm^{-2} at RT. The symmetrical Li/LBS/Li cell also shows good cycling stability for more than 140 h at a current density of 0.3 mA cm^{-2} and a charge/discharge capacity of 0.3 mAh cm^{-2}. Moreover, the ionic conductivity of the LBS solid electrolyte is stable, ensuring suitability for long-term storage and use. Our work provides the first comprehensive report on the electrochemical performance of lithium thioborates. This work accordingly provides an effective technique to synthesize single crystalline phase LBS with low mass density, fast ionic conduction, wide electrochemical stability window, and good cycling stability. In addition, this work provides guiding principles on synthesizing lithium thioborate derivative SSEs and promotes the further development and wider application of sulfide system solid electrolytes. Incorporating doping techniques to increase the ionic conductivity of LBS is also a promising research direction.

■ EXPERIMENTAL SECTION

Chemicals and Materials. Lithium sulfide (Li$_2$S, 99.9%, Alfa Aesar), boron powder (Amorphous, 95−97%, Alfa Aesar), sulfur (Sigma-Aldrich), indium foil (In, Alfa Aesar), and Li foil (Sigma-Aldrich) were used.

Synthesis of LBS Powder. Li$_2$S, boron powder, and sulfur powder with an appropriate ratio were mixed in a mortar to obtain a uniform precursor mixture. All handling of powders was carried out in Ar-filled glovebox. The precursor mixture was supported in a BN crucible, which was placed in a stainless-steel reactor and then sealed. After that, the reactor was taken out of the glovebox for sintering. The reactor was heated up to 750 °C in 4 h and held for 2 h, then cooled to 550 °C in 4 h and held for 12 h, cooled to 50 °C in 10 h with a cooling rate of 50 °C/h, and finally cooled to RT. Finally, the reactor was opened in the glovebox to collect the LBS powder.

Materials Characterizations. Synchrotron X-ray diffraction (XRD) measurement was carried out in capillary transmission mode at beamline 2-1 at the Stanford Synchrotron Radiation Lightsource (SSRL) with 17 keV beam energy and a Pilatus 100 K detector. The exact X-ray wavelength was refined to be 0.727873 Å based on data collected with LaB$_6$ standard reference material. The sample was loaded inside a 0.7 mm special glass capillary (Charles Supper) with one open end sealed with epoxy in a glovebox, and then flame-sealed to prevent air exposure. Rietveld refinement of the XRD data was performed using TOPAS-Academic (V7).[48] For the multiphase samples (presented in Table S2), a quick phase purity check was also performed by lab XRD employing PANalytical Empyrean with Mo Kα radiation in Bragg−Brentano configuration. These samples were placed in a domed sample holder (Anton Paar) in a glovebox before measurement to reduce air exposure. The Li/B ratio in the samples was determined by ICP-MS (Thermo

Scientific XSERIES 2 ICP-MS). SEM images were obtained with a Thermo Fisher Scientific Apreo S LoVac SEM. Transmission electron microscopy Cryo-EM experiments were performed on the FEI Titan 80−300 kV environmental (scanning) transmission electron microscope (STEM) operated at an accelerating voltage of 300 kV with an energy resolution of 1 eV. The instrument is equipped with an aberration corrector in the image-forming lens, which is tuned before each experiment. Low-magnification Cryo-EM images were acquired with the Gatan Oneview CMOS camera with a dose rate of over 1000 e$^-$ Å^{-2} s^{-1} and an exposure time for each image of around 0.4 s. High-magnification Cryo-EM images were acquired with the Gatan K3 direct-detection camera with a dose rate of 50 e$^-$ Å^{-2} s^{-1}. Eight frames were taken with an exposure time of 0.1 s per frame for each image. Cryo-STEM EELS characterization was performed with a C2 aperture of 50 mm, a beam current of 10 pA, a camera length of 48 mm, and a pixel dwell time of 20 ms. EELS spectra were acquired on a GIF Quantum 966 instrument with a dispersion of 0.25 eV/channel in Dual EELS mode. The low-loss was centered on the zero-loss peak and the core-loss was centered on the S L-edge. Thus, the Li K-, S L-, and B K-edges can be simultaneously acquired. Energy drift during spectrum imaging was corrected by centering the zero-loss peak to 0 eV at each pixel. Maps were computed through a two-window method, with a pre-edge window fitted to a power-law background and a post-edge window of 10−20 eV on the core-loss signal.

Electrochemical Characterizations. The electrochemical properties were tested in customized pressure-controlled cells in an Ar-filled glovebox. In/LBS/In cells were fabricated to test the ionic conductivity: The LBS powder was pressed into a pellet (diameter: 13 mm; thickness: 0.5 mm) under 360 MPa for 2 min in a PEEK tank. After that, two In foils with a diameter of 9 mm were attached on both sides of the solid electrolyte pellet. The formed In/LBS/In cell was then sandwiched between two stainless steel rods which function as current collectors (Figure 4a is only for schematic purposes). The electrochemical impedance spectroscopy was measured under 35 MPa at RT. Li/LBS/LBS-graphite cells were fabricated to measure the CV: 100 mg LBS and 10 mg LBS-graphite powder (LBS powder: graphite is 75:25 in weight, on top of LBS powders) were cold-pressed together under 360 MPa (diameter: 6 mm; thickness: ∼2 mm), then a Li foil was attached on the other side of the pressed pellet. The formed Li/LBS/LBS-graphite cell was then sandwiched between two stainless steel rods which function as current collectors. The CVs of the Li/LBS/LBS-graphite cells were measured with a scan rate of 0.1 mV/s at RT under 35 MPa. The scanning voltage window was 1.0−4.0 V for oxidation and 0−1.8 V for reduction. Symmetrical Li/LBS/Li cells were fabricated to test the cycling stability: The LBS powder was pressed into a pellet (diameter: 6 mm; thickness: 0.5 mm) under 360 MPa for 2 min in a PEEK tank. After that, two Li foils with a diameter of 6 mm were attached on both sides of the LBS pellet. The formed Li/LBS/Li cell was then sandwiched between two stainless steel rods which function as current collectors. Galvanostatic cycling of the Li/LBS/Li cells was measured at RT under a cycling pressure of 35 MPa.

Simulation Methods. For the simulation of DFT-MD in Li$_{10}$B$_{10}$S$_{19}$, we utilized the Vienna ab initio simulation package (VASP) with the GGA of PBE and the PAW method. Our simulations used the NVT canonical ensemble. We simulated the structure as observed experimentally in this work, which

contains 312 total atoms. We used the Li_sv, B, and S pseudopotentials, a plane wave cutoff energy of 499 eV for all structures, and a gamma-point-only k-mesh. The VASP input files were generated using the *pymatgen.io.vasp.sets* module of Pymatgen.

To better understand Li diffusion pathways through the $Li_8B_{10}S_{19}$ phase, heat maps of Li atom position throughout the DFT-MD simulation were generated and are displayed in Figure 3. In these heatmaps, the positions of all Li atoms over all time steps are aggregated and visualized. For each of the three Cartesian directions, probability density functions are constructed from the number of Li atoms that crossed each coordinate in the 2D plane perpendicular to each axis. These density plots indicate where Li atoms spend most of their time; due to the speed of Li hopping between sites, exact pathways are not resolved. However, in combination with the diffusivity plots, which show significant isotropic diffusion, and the crystal structure, we can identify diffusion pathways throughout the material.

◼ ASSOCIATED CONTENT

Ⓢ Supporting Information

The Supporting Information is available free of charge at https://pubs.acs.org/doi/10.1021/acsenergylett.3c00560.

> Details on the Rietveld refinement and crystal structure; SEM images of the LBS particle, low-dose cryo-TEM image of the LBS particle, and high-resolution cryo-TEM image of LBS particle (inset shows FFT); STEM and EELS data of the LBS particle; experimental electrochemical stability windows of various sulfide electrolytes in the cells of Li|SSE|SSE+C; the synthesis products and their XRD patterns under different synthesis parameters including the synthesis atmosphere, molar ratio of raw materials, temperatures, and duration (PDF)

◼ AUTHOR INFORMATION

Corresponding Authors

Evan J. Reed − *Department of Materials Science and Engineering, Stanford University, Stanford, California 94305, USA*; Email: evanreed@stanford.edu

William C. Chueh − *Department of Materials Science and Engineering and Department of Chemistry, Stanford University, Stanford, California 94305, USA; Stanford Institute for Materials and Energy Sciences, SLAC National Accelerator Laboratory, Menlo Park, California 94025, USA*; ⓞ orcid.org/0000-0002-7066-3470; Email: wchueh@stanford.edu

Yi Cui − *Department of Materials Science and Engineering and Department of Chemistry, Stanford University, Stanford, California 94305, USA; Stanford Institute for Materials and Energy Sciences, SLAC National Accelerator Laboratory, Menlo Park, California 94025, USA*; ⓞ orcid.org/0000-0002-6103-6352; Email: yicui@stanford.edu

Authors

Yinxing Ma − *Department of Materials Science and Engineering, Stanford University, Stanford, California 94305, USA; College of Chemistry and Chemical Engineering, iChEM, Xiamen University, Xiamen 361005, People's Republic of China*

Jiayu Wan − *Department of Materials Science and Engineering, Stanford University, Stanford, California 94305, USA*; ⓞ orcid.org/0000-0003-4603-3265

Xin Xu − *Department of Materials Science and Engineering, Stanford University, Stanford, California 94305, USA*; ⓞ orcid.org/0000-0002-5393-9412

Austin D. Sendek − *Department of Materials Science and Engineering, Stanford University, Stanford, California 94305, USA; Aionics, Inc., Palo Alto, California 94301, USA*

Sarah E. Holmes − *Department of Chemistry, Stanford University, Stanford, California 94305, USA*; ⓞ orcid.org/0000-0002-7946-964X

Brandi Ransom − *Department of Materials Science and Engineering, Stanford University, Stanford, California 94305, USA*; ⓞ orcid.org/0000-0002-9041-6725

Zhelong Jiang − *Department of Materials Science and Engineering, Stanford University, Stanford, California 94305, USA*; ⓞ orcid.org/0000-0003-0013-0860

Pu Zhang − *Department of Materials Science and Engineering, Stanford University, Stanford, California 94305, USA*

Xin Xiao − *Department of Materials Science and Engineering, Stanford University, Stanford, California 94305, USA*; ⓞ orcid.org/0000-0003-1098-9484

Wenbo Zhang − *Department of Materials Science and Engineering, Stanford University, Stanford, California 94305, USA*; ⓞ orcid.org/0000-0002-0828-594X

Rong Xu − *Department of Materials Science and Engineering, Stanford University, Stanford, California 94305, USA*; ⓞ orcid.org/0000-0002-3694-595X

Fang Liu − *Department of Materials Science and Engineering, Stanford University, Stanford, California 94305, USA*

Yusheng Ye − *Department of Materials Science and Engineering, Stanford University, Stanford, California 94305, USA*; ⓞ orcid.org/0000-0001-9832-2478

Emma Kaeli − *Department of Materials Science and Engineering, Stanford University, Stanford, California 94305, USA*

Complete contact information is available at:
https://pubs.acs.org/10.1021/acsenergylett.3c00560

Author Contributions

[†]Y.M., J.W., and X.X. contributed equally to this paper.

Notes

The authors declare no competing financial interest.

◼ ACKNOWLEDGMENTS

◼ REFERENCES

(1) Chen, R.; Li, Q.; Yu, X.; Chen, L.; Li, H. Approaching Practically Accessible Solid-State Batteries: Stability Issues Related to Solid Electrolytes and Interfaces. *Chem. Rev.* **2020**, *120* (14), 6820−6877.

(2) Lin, D.; Liu, Y.; Cui, Y. Reviving the lithium metal anode for high-energy batteries. *Nat. Nanotechnol.* **2017**, *12* (3), 194−206.

(3) Banerjee, A.; Wang, X.; Fang, C.; Wu, E. A.; Meng, Y. S. Interfaces and Interphases in All-Solid-State Batteries with Inorganic Solid Electrolytes. *Chem. Rev.* **2020**, *120* (14), 6878−6933.

(4) Tan, D. H. S.; Banerjee, A.; Chen, Z.; Meng, Y. S. From nanoscale interface characterization to sustainable energy storage using all-solid-state batteries. *Nat. Nanotechnol.* **2020**, *15* (3), 170−180.

(5) Randau, S.; Weber, D. A.; Kötz, O.; Koerver, R.; Braun, P.; Weber, A.; Ivers-Tiffée, E.; Adermann, T.; Kulisch, J.; Zeier, W. G.; Richter, F. H.; Janek, J. Benchmarking the performance of all-solid-state lithium batteries. *Nat. Energy* **2020**, *5* (3), 259−270.

(6) Manthiram, A.; Yu, X.; Wang, S. Lithium battery chemistries enabled by solid-state electrolytes. *Nat. Rev. Mater.* **2017**, *2* (4), 16103.

(7) Chen, X.; Xie, J.; Zhao, X.; Zhu, T. Electrochemical Compatibility of Solid-State Electrolytes with Cathodes and Anodes for All-Solid-State Lithium Batteries: A Review. *Adv. Energy Sustainability Res.* **2021**, *2*, 2000101.

(8) Fan, L.-Z.; He, H.; Nan, C.-W. Tailoring inorganic−polymer composites for the mass production of solid-state batteries. *Nat. Rev. Mater.* **2021**, *6* (11), 1003−1019.

(9) Azhari, L.; Bong, S.; Ma, X.; Wang, Y. Recycling for All Solid-State Lithium-Ion Batteries. *Matter* **2020**, *3* (6), 1845−1861.

(10) Zhao, Q.; Stalin, S.; Zhao, C.-Z.; Archer, L. A. Designing solid-state electrolytes for safe, energy-dense batteries. *Nat. Rev. Mater.* **2020**, *5* (3), 229−252.

(11) Gao, Z.; Sun, H.; Fu, L.; Ye, F.; Zhang, Y.; Luo, W.; Huang, Y. Promises, Challenges, and Recent Progress of Inorganic Solid-State Electrolytes for All-Solid-State Lithium Batteries. *Adv. Mater.* **2018**, *30* (17), 1705702.

(12) Kim, K. J.; Balaish, M.; Wadaguchi, M.; Kong, L.; Rupp, J. L. M. Solid-State Li−Metal Batteries: Challenges and Horizons of Oxide and Sulfide Solid Electrolytes and Their Interfaces. *Adv. Energy Mater.* **2021**, *11* (1), 2002689.

(13) Albertus, P.; Anandan, V.; Ban, C.; Balsara, N.; Belharouak, I.; Buettner-Garrett, J.; Chen, Z.; Daniel, C.; Doeff, M.; Dudney, N. J.; Dunn, B.; Harris, S. J.; Herle, S.; Herbert, E.; Kalnaus, S.; Libera, J. A.; Lu, D.; Martin, S.; McCloskey, B. D.; McDowell, M. T.; Meng, Y. S.; Nanda, J.; Sakamoto, J.; Self, E. C.; Tepavcevic, S.; Wachsman, E.; Wang, C.; Westover, A. S.; Xiao, J.; Yersak, T. Challenges for and Pathways toward Li-Metal-Based All-Solid-State Batteries. *ACS Energy Lett.* **2021**, *6* (4), 1399−1404.

(14) Xu, L.; Lu, Y.; Zhao, C. Z.; Yuan, H.; Zhu, G. L.; Hou, L. P.; Zhang, Q.; Huang, J. Q. Toward the Scale-Up of Solid-State Lithium Metal Batteries: The Gaps between Lab-Level Cells and Practical Large-Format Batteries. *Adv. Energy Mater.* **2021**, *11* (4), 2002360.

(15) Famprikis, T.; Canepa, P.; Dawson, J. A.; Islam, M. S.; Masquelier, C. Fundamentals of inorganic solid-state electrolytes for batteries. *Nat. Mater.* **2019**, *18* (12), 1278−1291.

(16) Kato, Y.; Hori, S.; Saito, T.; Suzuki, K.; Hirayama, M.; Mitsui, A.; Yonemura, M.; Iba, H.; Kanno, R. High-power all-solid-state batteries using sulfide superionic conductors. *Nat. Energy* **2016**, *1* (4), 16030.

(17) Kamaya, N.; Homma, K.; Yamakawa, Y.; Hirayama, M.; Kanno, R.; Yonemura, M.; Kamiyama, T.; Kato, Y.; Hama, S.; Kawamoto, K.; Mitsui, A. A lithium superionic conductor. *Nat. Mater.* **2011**, *10* (9), 682−686.

(18) Lau, J.; DeBlock, R. H.; Butts, D. M.; Ashby, D. S.; Choi, C. S.; Dunn, B. S. Sulfide Solid Electrolytes for Lithium Battery Applications. *Adv. Energy Mater.* **2018**, *8* (27), 1800933.

(19) Lee, Y.-G.; Fujiki, S.; Jung, C.; Suzuki, N.; Yashiro, N.; Omoda, R.; Ko, D.-S.; Shiratsuchi, T.; Sugimoto, T.; Ryu, S.; Ku, J. H.; Watanabe, T.; Park, Y.; Aihara, Y.; Im, D.; Han, I. T. High-energy long-cycling all-solid-state lithium metal batteries enabled by silver-carbon composite anodes. *Nat. Energy* **2020**, *5* (4), 299−308.

(20) Kaup, K.; Assoud, A.; Liu, J.; Nazar, L. F. Fast Li-Ion Conductivity in Superadamantanoid Lithium Thioborate Halides. *Angew. Chem., Int. Ed.* **2021**, *60* (13), 6975−6980.

(21) Liang, Y.; Liu, H.; Wang, G.; Wang, C.; Ni, Y.; Nan, C. W.; Fan, L. Z. Challenges, interface engineering, and processing strategies toward practical sulfide-based all-solid-state lithium batteries. *InfoMat* **2022**, *4* (5), 12292.

(22) Wu, J.; Liu, S.; Han, F.; Yao, X.; Wang, C. Lithium/Sulfide All-Solid-State Batteries using Sulfide Electrolytes. *Adv. Mater.* **2021**, *33* (6), 2000751.

(23) Liu, H.; Liang, Y.; Wang, C.; Li, D.; Yan, X.; Nan, C. W.; Fan, L. Z. Priority and Prospect of Sulfide-Based Solid-Electrolyte Membrane. *Adv. Mater.* **2023**, e2206013.

(24) Sendek, A. D.; Antoniuk, E. R.; Cubuk, E. D.; Ransom, B.; Francisco, B. E.; Buettner-Garrett, J.; Cui, Y.; Reed, E. J. Combining Superionic Conduction and Favorable Decomposition Products in the Crystalline Lithium-Boron-Sulfur System: A New Mechanism for Stabilizing Solid Li-Ion Electrolytes. *ACS Appl. Mater. Interfaces* **2020**, *12* (34), 37957−37966.

(25) Grune, M.; Muller-Warmuth, W.; Hebel, P.; Krebs, B. Complex lithium dynamics in the novel thioborate $Li_5B_7S_{13}$ revealed by NMR relaxatron and lineshape studies. *Solid State Ion* **1995**, *78* (3−4), 305−313.

(26) Hiltmann, F.; Hebel, P.; Hammerschmidt, A.; Krebs, B. $Li_5B_7S_{13}$ and $Li_9B_{19}S_{33}$: Two lithium thioborates with novel highly polymeric anion networks. *Z. Anorg. Allg. Chem.* **1993**, *619*, 293−302.

(27) Hiltmann, F.; Jansen, C.; Krebs, B. Li_3BS_3 and $LiSrBS_3$: New orthothioborates with trigonal planar boron coordination. *Z. anorg. allg. Chem.* **1996**, *622*, 1508−1514.

(28) Kimura, T.; Inoue, A.; Nagao, K.; Inaoka, T.; Kowada, H.; Sakuda, A.; Tatsumisago, M.; Hayashi, A. Characteristics of a Li_3BS_3 Thioborate Glass Electrolyte Obtained via a Mechanochemical Process. *ACS Appl. Energy Mater.* **2022**, *5* (2), 1421−1426.

(29) Jansen, C.; Kuper, J.; Krebs, B. $Na_2B_2S_5$ and $Li_2B_2S_5$: Two Novel perthioborates with planar 1, 2, 4-Trithia-3,5-Diborolane rings. *Z. anorg. allg. Chem.* **1995**, *621*, 1322−1329.

(30) Hebel, P.; Krebs, B. Preparation, crystal structure and^{7}Li NMR of $Li_{6+2x}[B_{10}S_{18}]S_x$ ($x≈2$). *Solid State Ion* **1990**, *43*, 133−142.

(31) Richards, W. D.; Miara, L. J.; Wang, Y.; Kim, J. C.; Ceder, G. Interface Stability in Solid-State Batteries. *Chem. Mater.* **2016**, *28* (1), 266−273.

(32) Han, F.; Westover, A. S.; Yue, J.; Fan, X.; Wang, F.; Chi, M.; Leonard, D. N.; Dudney, N. J.; Wang, H.; Wang, C. High electronic conductivity as the origin of lithium dendrite formation within solid electrolytes. *Nat. Energy* **2019**, *4* (3), 187−196.

(33) Sendek, A. D.; Cubuk, E. D.; Antoniuk, E. R.; Cheon, G.; Cui, Y.; Reed, E. J. Machine Learning-Assisted Discovery of Solid Li-Ion Conducting Materials. *Chem. Mater.* **2019**, *31* (2), 342−352.

(34) Han, F.; Gao, T.; Zhu, Y.; Gaskell, K. J.; Wang, C. A Battery Made from a Single Material. *Adv. Mater.* **2015**, *27* (23), 3473−3483.

(35) Han, F.; Zhu, Y.; He, X.; Mo, Y.; Wang, C. Electrochemical Stability of $Li_{10}GeP_2S_{12}$ and $Li_7La_3Zr_2O_{12}$ Solid Electrolytes. *Adv. Energy Mater.* **2016**, *6* (8), 1501590.

(36) Ohta, S.; Kobayashi, T.; Asaoka, T. High lithium ionic conductivity in the garnet-type oxide $Li_{7−X} La_3(Zr_{2−X}, Nb_X)O_{12}$ (X = 0−2). *J. Power Sources* **2011**, *196* (6), 3342−3345.

(37) Rangasamy, E.; Liu, Z.; Gobet, M.; Pilar, K.; Sahu, G.; Zhou, W.; Wu, H.; Greenbaum, S.; Liang, C. An iodide-based $Li_7P_2S_8I$ superionic conductor. *J. Am. Chem. Soc.* **2015**, *137* (4), 1384−1387.

(38) Tian, Y.; Ding, F.; Zhong, H.; Liu, C.; He, Y.-B.; Liu, J.; Liu, X.; Xu, Q. $Li_{6.75}La_3Zr_{1.75}Ta_{0.25}O_{12}$@amorphous Li_3OCl composite electrolyte for solid state lithium-metal batteries. *Energy Stor. Mater.* **2018**, *14*, 49−57.

(39) Swamy, T.; Chen, X.; Chiang, Y.-M. Electrochemical Redox Behavior of Li Ion Conducting Sulfide Solid Electrolytes. *Chem. Mater.* **2019**, *31* (3), 707−713.

(40) Li, Y.; Li, J.; Cheng, J.; Xu, X.; Chen, L.; Ci, L. Enhanced Air and Electrochemical Stability of $Li_7P_3S_{11}$−Based Solid Electrolytes Enabled by Aliovalent Substitution of SnO_2. *Adv. Mater. Interfaces* **2021**, *8* (14), 2100368.

(41) Li, Y.; Cheng, J.; Li, J.; Zeng, Z.; Guo, Y.; Zhang, H.; Liu, H.; Xu, X.; Rao, Y.; Li, D.; Ci, L. Indium doped sulfide solid electrolyte

with tamed lithium dendrite and improved ionic conductivity for all-solid-state battery applications. *J. Power Sources* **2022**, *542*, 231794.

(42) Yu, P.; Ahmad, N.; Zeng, C.; Lv, L.; Dong, Q.; Yang, W. Tailored $Li_7P_3S_{11}$ Electrolyte by In_2S_3 Doping Suppresses Electrochemical Decomposition for High-Performance All-Solid-State Lithium−Sulfur Batteries. *ACS Appl. Energy Mater.* **2022**, *5* (11), 13429−13438.

(43) Yu, S.; Mertens, A.; Tempel, H.; Schierholz, R.; Kungl, H.; Eichel, R. A. Monolithic All-Phosphate Solid-State Lithium-Ion Battery with Improved Interfacial Compatibility. *ACS Appl. Mater. Interfaces* **2018**, *10* (26), 22264−22277.

(44) Tan, D. H. S.; Wu, E. A.; Nguyen, H.; Chen, Z.; Marple, M. A. T.; Doux, J.-M.; Wang, X.; Yang, H.; Banerjee, A.; Meng, Y. S. Elucidating Reversible Electrochemical Redox of Li_6PS_5Cl Solid Electrolyte. *ACS Energy Lett.* **2019**, *4* (10), 2418−2427.

(45) Xu, H.; Cao, G.; Shen, Y.; Yu, Y.; Hu, J.; Wang, Z.; Shao, G. Enabling Argyrodite Sulfides as Superb Solid-State Electrolyte with Remarkable Interfacial Stability Against Electrodes. *Energy Environ. Sci.* **2022**, *5* (3), 852−864.

(46) Taklu, B. W.; Nikodimos, Y.; Bezabh, H. K.; Lakshmanan, K.; Hagos, T. M.; Nigatu, T. A.; Merso, S. K.; Sung, H.-Y.; Yang, S.-C.; Wu, S.-H.; Su, W.-N.; Hwang, B. J. Air-stable iodized-oxychloride argyrodite sulfide and anionic swap on the practical potential window for all-solid-state lithium-metal batteries. *Nano Energy* **2023**, *112*, 108471.

(47) Wang, C.; Fu, K.; Kammampata, S. P.; McOwen, D. W.; Samson, A. J.; Zhang, L.; Hitz, G. T.; Nolan, A. M.; Wachsman, E. D.; Mo, Y.; Thangadurai, V.; Hu, L. Garnet-Type Solid-State Electrolytes: Materials, Interfaces, and Batteries. *Chem. Rev.* **2020**, *120* (10), 4257−4300.

(48) Perl, J.; Shin, J.; Schumann, J.; Faddegon, B.; Paganetti, H. TOPAS: an innovative proton Monte Carlo platform for research and clinical applications. *Med. Phys.* **2012**, *39* (11), 6818−6837.

📖 Recommended by ACS